ELSEVIER

Journal of Fluids and Structures 24 (2008) 313–335

JOURNAL OF FLUIDS AND STRUCTURES

www.elsevier.com/locate/jfs

Numerical study of rowing hydrofoil performance at low Reynolds numbers

M.-H. Chung*

Institute of Ocean Engineering and Technology, National Kaohsiung Marine University, Kaohsiung City 81143, Taiwan, ROC

Received 4 July 2006; accepted 20 August 2007
Available online 26 November 2007

Abstract

In this paper, the hydrodynamic performance of a 2-D flat-plate hydrofoil in rowing motion is numerically studied by a Cartesian grid method with the cut-cell approach. Adaptive mesh refinement is used to save on the number of mesh cells without harming spatial resolution in critical regions. The rowing kinematics of the hydrofoil is the same for all simulations in this work. The design parameters studied are the reduced frequency of the rowing motion, the heave amplitude, and the time lags of the feathered-to-broadside rotation and the broadside-to-feathered rotation. Results show that larger thrust and efficiency can be attained if the feathered-to-broadside rotation is started right after the beginning of the power stroke and the broadside-to-feathered rotation is finished right before the end of the power stroke. Finally, both the thrust and the efficiency increase with Reynolds number.

Keywords: Rowing hydrofoil; Low Reynolds number; Cartesian grid method; Cut-cell approach; Adaptive mesh refinement

1. Introduction

In the course of the development of aircraft and underwater vehicles, bird flight and fish swimming have been inspiring and guiding the engineers and scientists in the field of aerodynamics and hydrodynamics. Over the years, the science of biomimetics has been established and structured through the previous works of many researchers. For these man-made machines, the propulsion system plays a significant role which needs the knowledge and integration of hydrodynamics, structural mechanics, control theory, etc. For locomotion in water, propulsion by hydrofoil motion is very common. The types of motion can be put into two major categories. The first is the "flapping" motion, similar to the *thunniform* mode of fish swimming (Breder, 1926; Lindsey, 1978). The thunniform mode belongs to the body/caudal fin (BCF) propulsion and is by far the most efficient locomotion mode evolved in the aquatic environment, where thrust is generated with a lift-based method, allowing high cruising speeds to be maintained for long periods. Significant lateral movements occur only at the caudal fin (producing more than 90% of the thrust) and at the area near the narrow peduncle. Although the design of thunniform swimmers is optimized for high-speed swimming in calm waters, it is particularly inefficient for other actions such as slow swimming, turning maneuvers and rapid acceleration from stationary, as well as for turbulent water. The second is the "rowing" motion which is one of the chief ingredients in the *labriform* mode of fish swimming (Breder, 1926; Lindsey, 1978). The labriform mode belongs to the median/paired fin

*Tel.: +886 7 3617141x3076; fax: +886 7 3602897.
E-mail addresses: mhsuan@mail.nkmu.edu.tw, meng.hsuan.chung@gmail.com

0889-9746/$ - see front matter
doi:10.1016/j.jfluidstructs.2007.08.008

(MPF) propulsion and is achieved by oscillatory movements of the pectoral fins. Blake (1983) identified two main oscillatory movement types for the pectoral fins: (i) a 'rowing' action (drag-based labriform mode) and (ii) a 'flapping' action (lift-based labriform mode). Drag-based methods are more relevant at slow speeds, while lift-based methods are more efficient at all flow speeds. Fins rarely perform a purely rowing or flapping movement; instead, a combination of the two, depending on the swimming speed, is used. It is estimated that about 15% of the fish families use non-BCF modes as their routine propulsive means, while a much greater number that typically rely on BCF modes for propulsion employ MPF modes for maneuvering and stabilization (Videler, 1993).

For real fish, the following swimming mode must be mentioned for completeness. That is, the BCF transient mode for fast starts or turns. Harper and Blake (1990) showed that fast-start acceleration of pike is significantly higher than that of trout for all performance parameters measured. They found that escape fast-start performance is related to body form. And their results support previous suggestions (Weihs, 1973; Lighthill, 1975; Webb, 1986) that the body form of pike is well-designed for BCF transient swimming and that of rainbow trout a compromise, showing some features that enhance BCF periodic (steady) swimming and some that benefit fast-start performance.

For the flapping motion, the following simple pitch-and-plunge (or heave) motion is most considered in the literature:

$$h = h_1 \sin(2\pi f_m t), \tag{1}$$

$$\alpha = \alpha_0 + \alpha_1 \sin(2\pi f_m t + \phi), \tag{2}$$

where h_1 is the plunge (or heave) amplitude, α_0 the mean pitch angle, α_1 the amplitude of the sinusoidal pitch angle variation, f_m the flapping frequency and ϕ the phase difference between the pitch-and-plunge motions. There has been a lot of experimental work to study and understand the basic mechanisms of force production and flow manipulation in oscillating (mostly flapping) foils for underwater use (Triantafyllou et al., 2004). The most comprehensive numerical investigations of the design parameter space are given by Isogai et al. (1999), Tuncer and Platzer (2000), and Ramamurti et al. (2001). All employed an NACA 0012 airfoil and solved the Reynolds averaged Navier–Stokes (RANS) equations. Isogai et al. (1999) and Tuncer and Platzer (2000) addressed compressible flows on a structured grid while Ramamurti et al. (2001) considered incompressible flows on an unstructured grid. The Reynolds number (Re) based on free-stream velocity and foil chord ranges from 10^3 to 10^5. All of them examined the effect of changing h_1, α_1, f, and ϕ on the average thrust coefficient and the thrust efficiency. Unfortunately, the results of Isogai et al. (1999) and Tuncer and Platzer (2000) differ by over 30% for some parameter combinations and the reason is not clear. Mittal (2004) argued that the turbulence modelling effects have to be examined. As for the results of Ramamurti et al. (2001), the computed thrust coefficient versus ϕ is generally consistent with the experiments of Anderson (1996) at $\mathrm{Re} = 1.1 \times 10^3$, but there is significant mismatch of thrust coefficient at higher frequencies with the experiments of Koochesfahani (1987) at $\mathrm{Re} = 1.2 \times 10^4$.

In contrast to the flapping motion, the rowing motion has received little attention in scientific research, neither in the numerical simulation nor in the experimental community. Though flapping motion is relevant for energy-efficient operation, such as is required during cruising, the rowing motion is more relevant to slow speed, maneuvering (starting, stopping, yawing, etc.) motion (Walker and Westneat, 2002). From a very crude pair of models of thrust-making device and assuming a constant drag and lift coefficient, Vogel (1996) calculated the average thrust, as a function of swimming speed, produced by the drag- and lift-based system, respectively. It was concluded that the drag-based system is very much better when the craft is nearly stationary but the lift-based system is clearly superior at higher swimming speeds. Recent blade-element computations (Walker and Westneat, 2000) also indicated that even though flapping motion is more efficient at all flow speeds, higher thrust can be generated at low speeds through a rowing motion. However, little is known about the wake topologies and other flow details for fins undergoing a rowing motion.

In this paper, a computational fluid dynamics research code based on the Cartesian cut-cell approach with adaptive mesh refinement was used to study the unsteady flow past a rowing hydrofoil at Reynolds numbers up to 1000. The simulations at higher Reynolds numbers are tentatively not conducted due to the above-mentioned unclear discrepancies found in the previous works. The viscous flow past a flat-plate hydrofoil at various rowing frequencies, heave amplitudes, and other design parameters, was simulated. Results are presented mainly in terms of the average thrust and the thrust efficiency versus the design parameters. The effect of Reynolds number is also investigated. The thickness ratio of the flat plate is $\frac{1}{20}$, with each end rounded by a semi-circle. As noted by Vogel (1996), the force coefficients of the lift-based system are much more sensitive to the cross-sectional shape of the plate than those of the drag-based system. Also shown in the work of Wang (2000) is that the force coefficients of elliptical cylinders with different thickness have almost the same functional dependence on the angle of attack but different magnitude. Thus a sufficiently thin flat plate would fulfill the purpose of the present work to find the tendency or functional relations with the design parameters.

2. Governing equations of fluid flow

In this work, a single flat-plate hydrofoil performs rowing motion in an effectively unbounded region with an inflow stream. The incompressible fluid flow is governed by the Navier–Stokes equations. Taking the hydrofoil chord length (c) and the free-stream velocity (U_∞) as the characteristic length and velocity, respectively, the integral nondimensional equations of motion are given by

$$\oint_{cs} \mathbf{u}\cdot\mathbf{n}\,\mathrm{d}S = 0, \tag{3}$$

$$\frac{\partial}{\partial t}\int_{cv}\mathbf{u}\,\mathrm{d}V + \oint_{cs}\mathbf{u}(\mathbf{u}\cdot\mathbf{n})\,\mathrm{d}S = -\oint_{cs} p\ \mathbf{n}\,\mathrm{d}S + \frac{1}{\mathrm{Re}}\oint_{cs}\nabla\mathbf{u}\cdot\mathbf{n}\,\mathrm{d}S, \tag{4}$$

where cv and cs denote the control volume and control surface, respectively, and $\mathbf{n}$ is the outward unit vector normal to the control surface. The Reynolds number $\mathrm{Re}\equiv U_\infty c/\nu$, with ν being the kinematic viscosity of the fluid.

3. Kinematic parameters of rowing motion

Rowing motion is a combination of heaving and pitching motion. The hydrofoil heaves back and forth along an axis parallel to the inflow and has a feathered orientation (nominally parallel to the inflow) during the forward stroke (recovery stroke) and a broadside orientation (nominally normal to the inflow) during the backward stroke (power stroke). Assume the power stroke starts at $t = 0$ and the hydrofoil pitches about its mid-chord axis. A family of profiles can then be established for the heaving velocity ($\mathrm{d}h/\mathrm{d}t$) of the center of the hydrofoil as function of time:

$$\frac{\mathrm{d}h}{\mathrm{d}t} = \begin{cases} \frac{1}{2}V_p\left[1-\cos\left(\pi\dfrac{t}{T_{\mathrm{acc},p}}\right)\right], & 0\leqslant t<T_{\mathrm{acc},p},\\ V_p, & T_{\mathrm{acc},p}\leqslant t<T_p-T_{\mathrm{acc},p},\\ \frac{1}{2}V_p\left[1+\cos\left(\pi\dfrac{t-T_p+T_{\mathrm{acc},p}}{T_{\mathrm{acc},p}}\right)\right], & T_p-T_{\mathrm{acc},p}\leqslant t<T_p,\\ -\dfrac{1}{2}V_r\left[1-\cos\left(\pi\dfrac{t-T_p}{T_{\mathrm{acc},r}}\right)\right], & T_p\leqslant t<T_p+T_{\mathrm{acc},r},\\ -V_r, & T_p+T_{\mathrm{acc},r}\leqslant t<T_{\mathrm{cycle}}-T_{\mathrm{acc},r},\\ -\frac{1}{2}V_r\left[1+\cos\left(\pi\dfrac{t-T_{\mathrm{cycle}}+T_{\mathrm{acc},r}}{T_{\mathrm{acc},r}}\right)\right], & T_{\mathrm{cycle}}-T_{\mathrm{acc},r}\leqslant t\leqslant T_{\mathrm{cycle}}, \end{cases} \tag{5}$$

where

$$T_{\mathrm{cycle}} = T_p + T_r, \tag{6}$$

$$V_p = \frac{2h_1}{T_p - T_{\mathrm{acc},p}}, \tag{7}$$

$$V_r = \frac{2h_1}{T_r - T_{\mathrm{acc},r}}. \tag{8}$$

The notation T_p and V_p denote the elapsed times and the maximum heaving velocity for the power stroke respectively. T_r and V_r are the corresponding quantities for the recovery stroke; h_1 is the heave amplitude; $T_{\mathrm{acc},p}$ is the acceleration time for which the foil speed is increased from 0 to V_p in the power stroke and $T_{\mathrm{acc},r}$ is the acceleration time for which the foil speed is increased from 0 to V_r in the recovery stroke. The deceleration time is the same as the acceleration time for both strokes. These definitions are illustrated in Fig. 1.

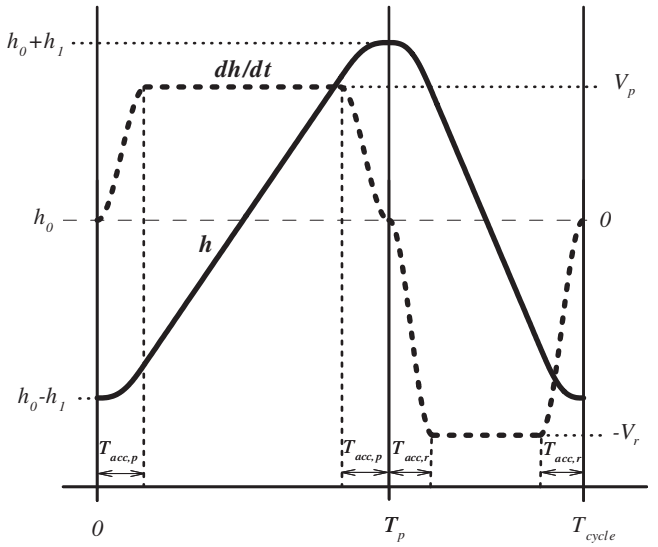

Fig. 1. Schematic showing the position (h) and the velocity ($\mathrm{d}h/\mathrm{d}t$) of the hydrofoil center as function of time.

Similarly, another family of profiles can be established for the pitching angle of attack (α) between the hydrofoil chord and the inflow direction:

$$\alpha(t)=\begin{cases}\alpha_0-\alpha_1, & 0\leqslant t<T_{lp}-T_{\alpha p},\\ \alpha_0+\alpha_1\sin\left[\pi\dfrac{t-T_{lp}}{2T_{\alpha p}}\right], & T_{lp}-T_{\alpha p}\leqslant t<T_{lp}+T_{\alpha p},\\ \alpha_0+\alpha_1, & T_{lp}+T_{\alpha p}\leqslant t<T_p+T_{lr}-T_{\alpha r},\\ \alpha_0-\alpha_1\sin\left[\pi\dfrac{t-T_p-T_{lr}}{2T_{\alpha r}}\right], & T_p+T_{lr}-T_{\alpha r}\leqslant t<T_p+T_{lr}+T_{\alpha r},\\ \alpha_0-\alpha_1, & T_p+T_{lr}+T_{\alpha r}\leqslant t<T_{\mathrm{cycle}}+T_{lp}-T_{\alpha p},\\ \alpha_0+\alpha_1\sin\left[\pi\dfrac{t-T_{lp}}{2T_{\alpha p}}\right], & T_{\mathrm{cycle}}+T_{lp}-T_{\alpha p}\leqslant t\leqslant T_{\mathrm{cycle}},\end{cases}\tag{9}$$

where α_0 and α_1 is the average and amplitude of the pitching angle of attack respectively; $2\,T_{\alpha p}$ is the time for which the foil rotates from the feathered ($\alpha_0-\alpha_1$) to the broadside orientation ($\alpha_0+\alpha_1$); $2\,T_{\alpha r}$ is the time for which the foil rotates from the broadside to the feathered orientation; T_{lp} is the time when the foil angle of attack increases to the average value from the minimum value, lagging behind the time when the power stroke begins; T_{lr} is the time when the foil angle of attack decreases to the average value from the maximum value, lagging behind the time when the recovery stroke begins. These definitions are illustrated in Fig. 2.

The corresponding position of the hydrofoil center (h) and the angular velocity of the hydrofoil ($\mathrm{d}\alpha/\mathrm{d}t$) as function of time can thus be derived from Eqs. (5) and (9), respectively, as

$$h(t)=\begin{cases}h_{\min}+\frac{1}{2}V_p\left[t-\dfrac{T_{\mathrm{acc},p}}{\pi}\sin\left(\pi\dfrac{t}{T_{\mathrm{acc},p}}\right)\right], & 0\leqslant t<T_{\mathrm{acc},p},\\ h_{\min}-\frac{1}{2}V_p\cdot T_{\mathrm{acc},p}+V_p\cdot t, & T_{\mathrm{acc},p}\leqslant t<T_p-T_{\mathrm{acc},p},\\ h_{\min}+V_p\left(\dfrac{1}{2}T_p-T_{\mathrm{acc},p}\right)+\frac{1}{2}V_p\left[t+\dfrac{T_{\mathrm{acc},p}}{\pi}\sin\left(\pi\dfrac{t-T_p+T_{\mathrm{acc},p}}{T_{\mathrm{acc},p}}\right)\right], & T_p-T_{\mathrm{acc},p}\leqslant t<T_p,\\ h_{\max}+\frac{1}{2}V_r\cdot T_p-\frac{1}{2}V_r\left[t-\dfrac{T_{\mathrm{acc},r}}{\pi}\sin\left(\pi\dfrac{t-T_p}{T_{\mathrm{acc},r}}\right)\right], & T_p\leqslant t<T_p+T_{\mathrm{acc},r},\\ h_{\max}+V_r\left(T_p+\frac{1}{2}T_{\mathrm{acc},r}\right)-V_r\cdot t, & T_p+T_{\mathrm{acc},r}\leqslant t<T_{\mathrm{cycle}}-T_{\mathrm{acc},r},\\ h_{\min}+\frac{1}{2}V_r\cdot T_{\mathrm{cycle}}-\frac{1}{2}V_r\left[t+\dfrac{T_{\mathrm{acc},r}}{\pi}\sin\left(\pi\dfrac{t-T_{\mathrm{cycle}}+T_{\mathrm{acc},r}}{T_{\mathrm{acc},r}}\right)\right], & T_{\mathrm{cycle}}-T_{\mathrm{acc},r}\leqslant t\leqslant T_{\mathrm{cycle}},\end{cases}\tag{10}$$

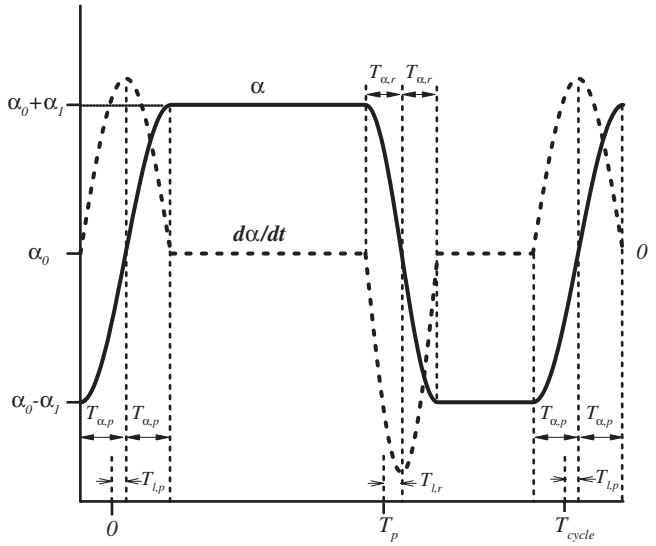

Fig. 2. Schematic showing the pitching angle of attack (α) and the angular velocity ($d\alpha/dt$) of the hydrofoil as function of time.

$$\frac{d\alpha}{dt}=\begin{cases}0, & 0\leqslant t<T_{lp}-T_{\alpha p},\\ \alpha_1\dfrac{\pi}{2T_{\alpha p}}\cos\left[\pi\dfrac{t-T_{lp}}{2T_{\alpha p}}\right], & T_{lp}-T_{\alpha p}\leqslant t<T_{lp}+T_{\alpha p},\\ 0, & T_{lp}+T_{\alpha p}\leqslant t<T_p+T_{lr}-T_{\alpha r},\\ -\alpha_1\dfrac{\pi}{2T_{\alpha r}}\cos\left[\pi\dfrac{t-T_p-T_{lr}}{2T_{\alpha r}}\right], & T_p+T_{lr}-T_{\alpha r}\leqslant t<T_p+T_{lr}+T_{\alpha r},\\ 0, & T_p+T_{lr}+T_{\alpha r}\leqslant t<T_{\text{cycle}}+T_{lp}-T_{\alpha p},\\ \alpha_1\dfrac{\pi}{2T_{\alpha p}}\cos\left[\pi\dfrac{t-T_{lp}}{2T_{\alpha p}}\right], & T_{\text{cycle}}+T_{lp}-T_{\alpha p}\leqslant t\leqslant T_{\text{cycle}},\end{cases}\tag{11}$$

where

$$h_{\min}=h_0-h_1,\tag{12}$$

$$h_{\max}=h_0+h_1,\tag{13}$$

and h_0 is the average position of the hydrofoil center.

In this work, the focus of interest is the effects of the normalized heave amplitude $h_1^*\equiv h_1/c$, reduced frequency $k\equiv 2\pi c/(U_\infty T_{\text{cycle}})$, and the normalized time lags $T_{lp}^*\equiv T_{lp}/T_{\text{cycle}}$ and $T_{lr}^*\equiv T_{lr}/T_{cycle}$. The other parameters are fixed for all simulations. They are

$$\alpha_0=\alpha_1=45^\circ,\tag{14}$$

$$T_p=T_r=0.5\ \ T_{\text{cycle}},\tag{15}$$

$$T_{\text{acc},p}=T_{\text{acc},r}=0.1\ \ T_{\text{cycle}},\tag{16}$$

$$T_{\alpha p}=T_{\alpha r}=0.05\ \ T_{\text{cycle}}.\tag{17}$$

That is, the feathered and broadside orientation are actually parallel and normal to the inflow, respectively, and a duty cycle of 50% is assumed. The corresponding maximum heaving velocities normalized by the inflow velocity are

$$V_p^*=V_r^*=2.5\,k\,h_1^*/\pi=2.5\,\text{St},\tag{18}$$

where the Strouhal number $\text{St}\equiv 2h_1/(U_\infty T_{\text{cycle}})$. Note that they are a little less than that occurring in the simple pitch-and-plunge motion defined by Eq. (1) i.e., πSt. The average position h_0 is not relevant, because the hydrofoil moves in an unbounded region.

4. Performance parameters

Thrust production is the main purpose of a rowing hydrofoil, therefore the magnitude of thrust and the efficiency of thrust generation are two important parameters quantifying and analyzing the hydrodynamic performance and the flow field. Thrust is the reaction of the drag force and the thrust coefficient is defined as

$$C_T = -C_D = 2T/(\rho U_\infty^2 c), \tag{19}$$

where T is the thrust and ρ the density of the fluid. The other performance parameters relevant to this work are the lift coefficient (C_L) and the moment coefficient (C_M):

$$C_L = 2L/(\rho U_\infty^2 c), \tag{20}$$

$$C_M = 2M/(\rho U_\infty^2 c^2), \tag{21}$$

where L is the lift force and M is the moment of hydrodynamic force about the pitching axis exerted by the fluid.

To elucidate the meaning of the thrust efficiency, note first that the instantaneous mechanical power input to the ambient fluid by the hydrofoil motion is

$$P(t) = T(t)\frac{\mathrm{d}h}{\mathrm{d}t} - M(t)\frac{\mathrm{d}\theta}{\mathrm{d}t}. \tag{22}$$

Only a portion of the acquired energy in the ambient fluid can contribute back to producing the thrust against the inflow, i.e., the useful power, TU_∞. The rest is lost and transferred in the form of kinetic energy to the fluid. Then a thrust efficiency (η), called the Froude efficiency after William Froude (1810–1879) who first used it, can be defined as the ratio of the useful power to the mechanical power input in an average sense:

$$\eta = \frac{\langle T\rangle U_\infty}{\langle P\rangle}, \tag{23}$$

where $\langle \cdot \rangle$ denotes the averaging operator over one period of motion,

$$\langle\cdot\rangle \equiv \frac{1}{T_{\mathrm{cycle}}}\int_{t_0}^{t_0+T_{\mathrm{cycle}}} \mathrm{d}t. \tag{24}$$

5. Numerical method

The governing equations, Eqs. (3) and (4), constitute a nonlinear and coupled system of differential equations. The cell-centered collocated finite volume pressure-free projection method combined with cut cell Cartesian approach is applied to discretize this set of coupled equations with immersed arbitrarily moving bodies. This method has been detailed and the computer code verified and validated extensively in the earlier work (Chung, 2006). It is modified in this work mainly in the following aspects.

First, only the first probing point on the reference normal line to the boundary segment is established, hence the evaluation of diffusion flux on the body surface turns out to be first-order accurate.

Second, if a previously negative (solid) cell center becomes positive (fluid) at the current time step, the numerical solution of the advection–diffusion equation for this cell is abandoned. Instead, the current cell center velocity is interpolated out from the neighboring solution nodes (Udaykumar et al., 1999) by the inverse distance scheme. Numerical experience showed that this modification would reduce the newborn cell related oscillations on the curve of drag or lift as function of time while hardly affecting the carrier curve.

Third, the adaptive mesh refinement (AMR) is introduced to use as few as possible mesh cells while not downgrading the spatial resolution in the relevant regions.

Fourth, due to the unstructured mesh numbering inherent in AMR, the solution stencil is no more compact and the strongly implicit procedure (SIP) used by Chung (2006) is not appropriate for solving the present system of algebraic equations formed by the linearized discretized governing equations. Instead, the Krylov subspace method is called for. The necessity imposed by SIP of explicit treatment for the far nodes in the solution stencil mentioned in Chung (2006) can now be relaxed by the Krylov subspace method.

It can be argued that the first two modifications only influence the accuracy of solution locally near the solid body, while the global superlinear order of accuracy (Chung, 2006) would not be destroyed. Therefore, the verification and

validation for these two modifications can be skipped reasonably. The last two modifications will be addressed in detail in the following subsections.

5.1. Adaptive mesh refinement

For accurately simulating the flow field around arbitrarily moving bodies, sufficiently fine meshes are called for in near-body regions and regions with complicated flow structures. However, the near-body region changes its location following the body motion and prior knowledge of locations of complicated flow regions is impossible even in a steady simulation. If the grid is fixed throughout the simulation, it is inevitable to lay fine meshes on the whole computational domain, causing an astonishingly high computational cost. The idea of AMR can overcome these difficulties. In the AMR approach, fine meshes are distributed only in the above two regions and coarse meshes in other regions. The number and distribution of fine and coarse meshes thus change with time. From the current to the next time step, if some fine meshes are judged to be merged into a coarser mesh (de-refinement), the variable value at the new mesh cell center is obtained by some sort of spatial average (restriction); if a coarse mesh is judged to be split into some finer meshes (refinement), the variable values at the new mesh cell centers is obtained by some sort of spatial interpolation (prolongation). Hence book-keeping is necessary to record the relation of inheritance between the two meshes for these two operations.

In this work, PARAMESH V2.0 (MacNeice et al., 2000) was adopted to implement the idea of AMR mainly due to ease of combining it with the in-house code. The computational domain is discretized by various hierarchical rectangular sub-grids which form the nodes of tree data-structure (quad-tree for 2-D and oct-tree for 3-D). If the spatial resolution in a sub-grid is judged to be increased, it turns out to be a parent grid block, spawns 4 (8 for 3-D) child grid blocks at one more refinement level, and hides behind. The prolongation of bilinear interpolation is used to evaluate the variable values at the center of each spawn grid block. If the spatial resolution in each of 4 (8 for 3-D) child grid blocks and their parent grid block is judged to be decreased, the child grid blocks merge and disappear with their parent grid block surfacing. The restriction of arithmetic mean is used to evaluate the variable values at the center of the surfacing grid block. A leaf grid block is defined as a newly spawn or surfacing grid block. Numerical computations are conducted only in leaf grid blocks. All the grid blocks have the same logical structure and cell number in each spatial dimension. They only differ in size, location, the parent block, and the list of neighboring and child blocks.

In this work, the cell number in each sub-grid block ($N_x \times N_y$) is fixed at (4×4). For grid blocks cut by or close to body surfaces, the refinement level is fixed at a constant number throughout the simulation, called the body refinement level (l_{body}). For other grid blocks, the basic criterion for refinement and de-refinement of a sub-grid block are, respectively, set to

$$\max_{i,j} |\omega_{i,j}| > 0.02\ \omega_{\max} \quad (i = 1, \ldots, N_x \text{ and } j = 1, \ldots, N_y), \tag{25}$$

$$\max_{i,j} |\omega_{i,j}| < 0.01\ \omega_{\max} \quad (i = 1, \ldots, N_x \text{ and } j = 1, \ldots, N_y), \tag{26}$$

where $\omega_{i,j}$ is the vorticity vector of cell (i,j) and $\omega_{\max}$ is the maximum magnitude of vorticity vector in the current flow field. In the near-body region, the maximum refinement level is l_{body}; in the bulk region off the body, a different maximum refinement level l_{bulk} is adopted. Usually $l_{\text{bulk}} < l_{\text{body}}$ to effectively reduce the total cell numbers. The near-body region is delimited by a collar zone which is an extension to the rectangular box defined by the extreme coordinates of the solid body surface; see Fig. 3.

Besides data passing from the previous to the current time step, the other complexity induced by applying the mesh refinement strategy is the flux evaluation at the interfaces between fine and coarse meshes in the finite volume method. In this work, a consistent scheme with compact stencil is devised to approximate this flux. As shown in Fig. 4, for a general variable ϕ,

$$\phi_{e_1} = \tfrac{1}{3}\phi_P + \tfrac{5}{6}\phi_{Q_1} - \tfrac{1}{6}\phi_{Q_2}, \quad \phi_{e_2} = \tfrac{1}{3}\phi_P - \tfrac{1}{6}\phi_{Q_1} + \tfrac{5}{6}\phi_{Q_2}, \tag{27}$$

$$\left(\frac{\partial \phi}{\partial x}\right)_{e_1} = \left(\frac{\partial \phi}{\partial x}\right)_{e_2} = \frac{1}{h_{Q,x}}\left(-\frac{2}{3}\phi_P + \frac{1}{3}\phi_{Q_1} + \frac{1}{3}\phi_{Q_2}\right), \tag{28}$$

where $h_{Q,x}$ is the fine mesh cell size in the x direction. These constitute the building-block formulas for various flux approximations at the fine mesh cell face "e_1" and "e_2". To assure the conservation of physical quantities, the flux on the full eastern cell face of the coarse mesh cell P is exactly the sum of those on the western cell face of the fine mesh cell Q_1 and Q_2. This scheme can be derived by regarding P, Q_1, and Q_2 as three nodes of a linear triangular element. In the Appendix, the order of accuracy for this scheme will be illustrated.

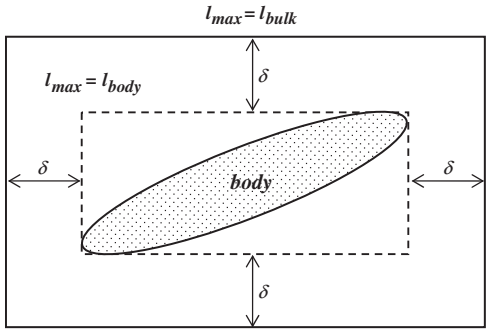

Fig. 3. Schematic showing the different selection of maximum refinement level. The dashed line defines the body rectangle zone to which the collar zone of width δ is extended. The two zones form the near-body region inside of which $l_{\max} = l_{\text{body}}$. In the exterior region $l_{\max} = l_{\text{bulk}}$.

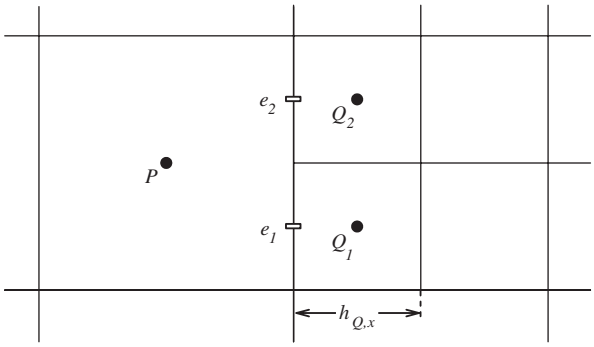

Fig. 4. Illustration for the flux evaluation at the interface between fine and coarse mesh in the finite volume method.

Finally, PARAMESH was originally designed and developed for astronomical computations (Antiochos et al., 1999), therefore the boundary conditions are far-field type. In this work, the formula of restriction and prolongation for the cells adjacent to the boundary of computational domain were modified to reflect the half-cell effect. Further, for parallel computation, the Morton reordering of sub-grid blocks in PARAMESH was designed to increase data locality, hence reduce the data passing time between processors. In view of serial computation of the in-house code used in this work, this reordering is disabled to save on the memory demand. The source code and license agreement of PARAMESH can be downloaded via the internet: http://ct.gsfc.nasa.gov/paramesh/Users_manual/amr.html.

5.2. Solution of the algebraic equations system

The system of linear algebraic equations generated for each solution variable has the form

$$\mathbf{A}\ \mathbf{x} = \mathbf{b}, \tag{29}$$

where $\mathbf{x}$ is the solution vector, $\mathbf{b}$ the source vector, and $\mathbf{A}$ the sparse and non compact irregularly structured coefficient matrix due to the unstructured mesh numbering inherent in AMR. This system can be efficiently solved by the Krylov subspace method. In this work, a basic tool kit for sparse matrix computations, the SPARSKIT, downloadable from http://www-users.cs.umn.edu/~saad/software/SPARSKIT/sparskit.html, was linked to the in-house code to do the iterative computations and associated matrix manipulations and operations. SPARSKIT supports a variety of data storage formats and the conversion routines between each other. Most of the routines in SPARSKIT use internally the compressed sparse row (CSR) format due to simplicity, generality, and widespread use. In this work, this basic format is used to store the nonzero elements of the coefficient matrix. Meanwhile, the mapping of data structure from PARAMESH to SPARSKIT was also established. From this tool kit, the restarted generalized minimal residual method (Saad and Schultz, 1986), called GMRES(m), is selected to solve the linear system which is right preconditioned by the incomplete LU factorization with dual truncation strategy (ILUT). Throughout the simulations in this work, the

choice of the dimension of Krylov subspace, m, is 3 for the u and v equations and 20 for the pressure Poisson equation. The relative dropping threshold in L and U is set at 5×10^{-3} for the u and v equations and 10^{-4} for the pressure Poisson equation. The number of fill-in elements in L and U is set at 60 for the u, v and the pressure Poisson equations. There are no definite rules for determining or optimizing these numerical values, hence they were settled by trial and error in this work. In GMRES(m), the Arnoldi procedure is used to construct an orthonormal basis for the Krylov subspace. The problem of minimizing the residual (a least squares problem) is solved by the QR decomposition method performed with transformation by a sequence of Givens rotations.

For the pressure Poisson equation, the convergence criterion is that the maximum of the residuals normalized by the cell volume, V_{cell}, over all the control volumes should be less than a prescribed value, usually 10^{-3} for unsteady simulations, i.e.,

$$\left\|\frac{\mathbf{A}\cdot\mathbf{x}-\mathbf{b}}{V_{\text{cell}}}\right\|_{\infty}<10^{-3}. \tag{30}$$

For the u and v equations, they must be solved in a coupled way because the fully implicit scheme is used for the advection–diffusion equation (Chung, 2006). That is, there is a loop for outer iteration. For each outer iteration, $\mathbf{A}$ is reestablished using the last updated mass flux and Eq. (29) is solved by m inner iterations of GMRES for the u and then v equation. A reasonable convergence criterion for the outer iteration is

$$\frac{\max_i|\phi_i^{l+1}-\phi_i^{l}|}{\max_i(\phi_i^{l+1})-\min_i(\phi_i^{l+1})}<10^{-3}, \tag{31}$$

where ϕ stands for u or v, i is the index of the solution node and l the loop count of the outer iteration.

6. Numerical results

At first, the computational domain to perform the simulations is $[-16,\,16]\times[-16,\,16]$. At the left boundary, an inflow velocity U_∞ is imposed. At the right boundary, the outflow condition is employed (Chung, 2006). The bottom and top boundaries are fully slippery and impermeable. The hydrofoil heaves back and forth along the x-axis. The average position of the hydrofoil center is $h_0=-4$. The simulation starts at $t=0$ when the hydrofoil center comes to the left-most position and the power stroke begins. Only the first period of motion is simulated. The width of the collar zone $\delta=0.25c$. The time step size obeys the CFL-like condition:

$$\Delta t=f\cdot\min\left[2\min_{i\in\text{fluid node}}\left(\min\left(\frac{\Delta x}{|u|},\frac{\Delta y}{|v|}\right)\right)_i\ \min_{i\in\text{solid boundary node}}\left(\min\left(\frac{\Delta x}{|u_{n,x}|},\frac{\Delta y}{|u_{n,y}|}\right)\right)_i\right], \tag{32}$$

where $f\leqslant1$ and $u_{n,x}$ and $u_{n,y}$ denote, respectively, the x- and y-component of the normal velocity at the solid boundary node.

In the following simulations, unless stated otherwise, $f=0.5$ and the two maximum refinement levels are $l_{\text{body}}=11$ and $l_{\text{bulk}}=9$, generating the minimum mesh size of $\frac{1}{128}$ and $\frac{1}{32}$, respectively. Fig. 5 shows the sub-grid block topology at selected instants for the case of $h_1^*=2$, $k=8$, and $T_{lp}^*=T_{lr}^*=0$ at $\text{Re}=1000$.

The range of design parameters studied in this work is listed in Table 1. Only a few combinations of them were selected to conduct simulations. The Reynolds number effect is investigated for only one combination via simulations at $\text{Re}=10$, 50, 100, 500, and 1000.

6.1. Convergence test

To test for convergence, three simulations were run: the first employs $f=0.5$, $l_{\text{body}}=11$ and $l_{\text{bulk}}=9$, the second $f=1$, $l_{\text{body}}=12$ and $l_{\text{bulk}}=10$, and the third $f=0.25$, $l_{\text{body}}=11$ and $l_{\text{bulk}}=9$. The first two are compared to test convergence in grid resolution and the first and the third to test convergence in time step size. For these simulations $\text{Re}=1000$ and the design parameters are $h_1^*=2$, $k=8$, and $T_{lp}^*=T_{lr}^*=0$. The computed thrust, lift, and moment coefficients as function of normalized time (t/T_{cycle}) are plotted in Fig. 6 with high-frequency oscillations filtered out. Note that those mesh-size scale oscillations existing in the raw data are directly related to the process of merging cells when a node switches from fluid to solid. The amplitude of oscillation is larger when the time step size is smaller because the cell shape deformation (cell volume increase) due to cell merging is bigger for a smaller time step size. Nevertheless, the high-frequency components do hardly influence the low-frequency ones, hence can be neglected. The curves of

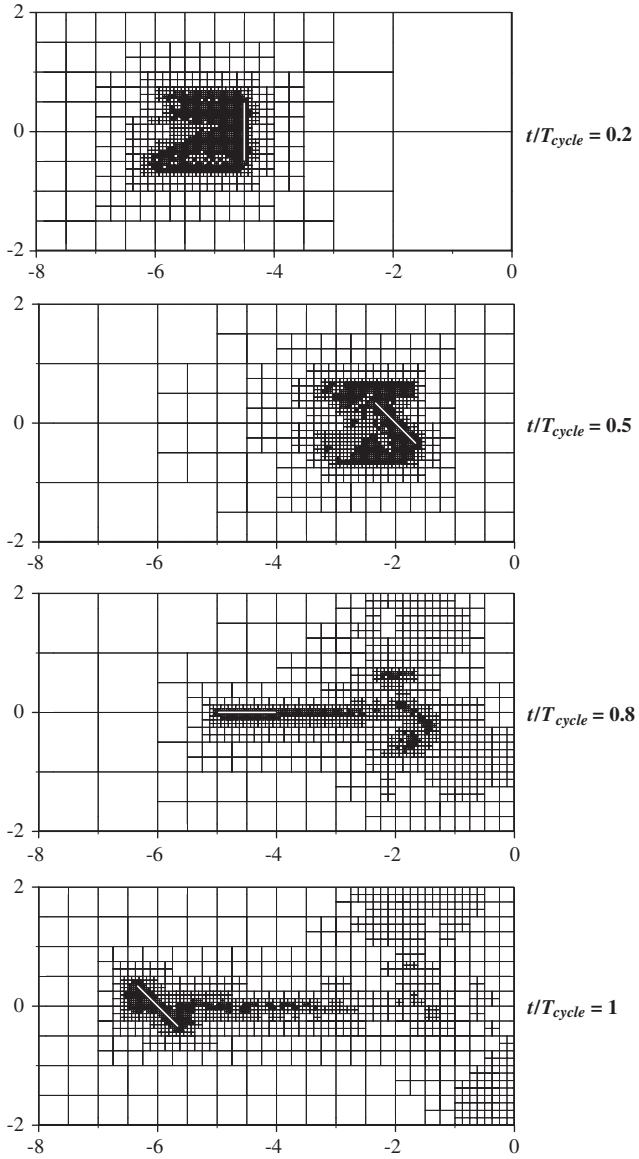

Fig. 5. Sub-grid block topology at selected instants for the case of $h_1^* = 2$, $k = 8$, and $T_{lp} = T_{lr} = 0$ at Re = 1000. Note that each sub-grid block has 4×4 mesh cells.

Table 1
Range of design parameters studied

h_1^*	k	T_{lp}^*	T_{lr}^*
1, 2, 4	1, 2, 4, 6, 8	−0.05, 0, 0.05, 0.1	−0.15, −0.1, −0.05, 0, 0.05

thrust coefficient show very good agreement. For the lift and moment coefficients the convergence is acceptable. Table 2 presents various average, minimal, and maximal hydrodynamic coefficients and the thrust efficiency obtained from these smoothed curves. Also shown are the corresponding percentage maximal differences among the three simulation cases. Again, the convergence is satisfactory, especially the averaged quantities. Therefore, the grid resolution and the

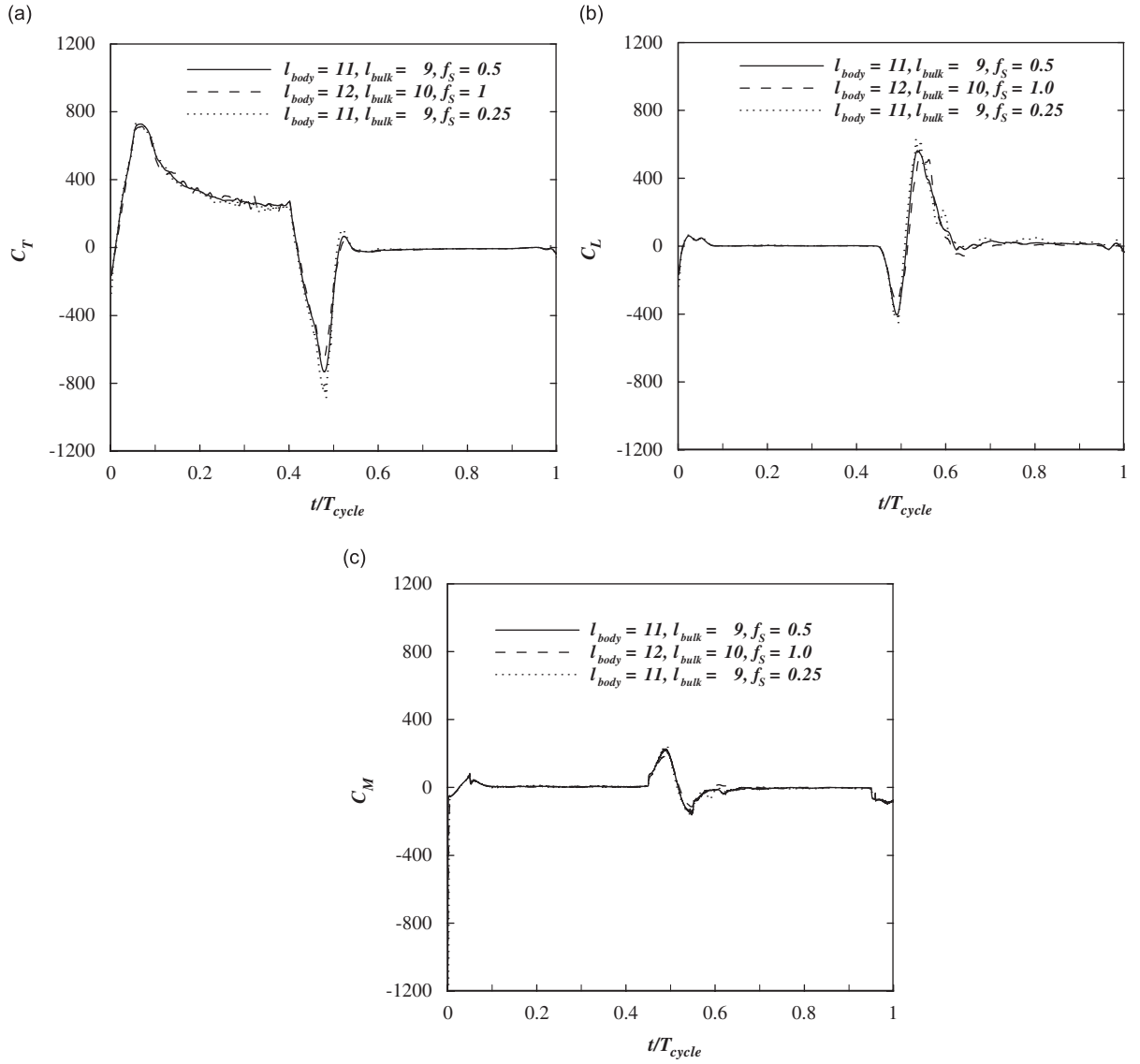

Fig. 6. Convergence test in grid resolution and time step size in terms of average hydrodynamic performance.

time step size used in the first simulation ($f = 0.5$, $l_{\text{body}} = 11$ and $l_{\text{bulk}} = 9$) were employed to conduct all the other simulations in this work for the sake of saving computational cost.

6.2. *Effect of normalized heave amplitude h_1^* and reduced frequency k*

The first parameter study is to examine the effect of normalized heave amplitude (h_1^*) and reduced frequency (k) on various hydrodynamic performances at Re = 1000. For simulations in this subsection, h_1^* is varied from 1 to 4, k from 1 to 8 and the other parameters kept constant ($T_{lp}^* = T_{lr}^* = 0$). The result is presented in terms of performance parameter as function of the Strouhal number (St).

Fig. 7 shows the average thrust coefficient as function of the Strouhal number for different normalized heave amplitudes. The data collapse is very good, compared with the data of 2-D flapping foil computed by Tuncer and Platzer (2000). Moreover, the average thrust coefficient increases in a nearly quadratic manner with the Strouhal

Table 2
Results of the convergence test in grid resolution and time step size

Case	$\langle C_T \rangle$	$C_{T,\min}$	$C_{T,\max}$	$\langle C_L \rangle$	$C_{L,\min}$	$C_{L,\max}$	$\langle C_M \rangle$	$C_{M,\min}$	$C_{M,\max}$	η
(1)										
$f = 0.5$										
$l_{body} = 11$	104.92	−731.48	728.06	25.10	−401.19	556.09	1.22	−137.45	219.91	0.0567
$l_{bulk} = 9$										
(2)										
$f = 1.0$										
$l_{body} = 12$	105.47	−663.87	712.96	18.85	−323.46	503.11	2.58	−107.78	183.42	0.0571
$l_{bulk} = 10$										
(3)										
$f = 0.25$										
$l_{body} = 11$	98.82	−882.96	733.48	31.24	−451.64	629.27	0.39	−157.81	231.94	0.0568
$l_{bulk} = 9$										
ε_F (%)	0.45	14.76	1.38	1.30	13.42	13.21	0.63	14.46	14.02	0.57

For the hydrodynamic coefficients, the maximal difference

$$\varepsilon_{F_i} \equiv \frac{\max\limits_{\text{case}=1,3}(F_i)_{\text{case}} - \min\limits_{\text{case}=1,3}(F_i)_{\text{case}}}{\text{average}\limits_{\text{case}=1,3}(C_{i,\max} - C_{i,\min})}, \quad i = T, L, M \text{ and } F_i = \langle C_i \rangle, C_{i,\min}, C_{i,\max}.$$

For the thrust efficiency, $\varepsilon_\eta \equiv \dfrac{\max\limits_{\text{case}=1,3}(\eta)_{\text{case}} - \min\limits_{\text{case}=1,3}(\eta)_{\text{case}}}{\text{average}\limits_{\text{case}=1,3}(\eta)_{\text{case}}}$.

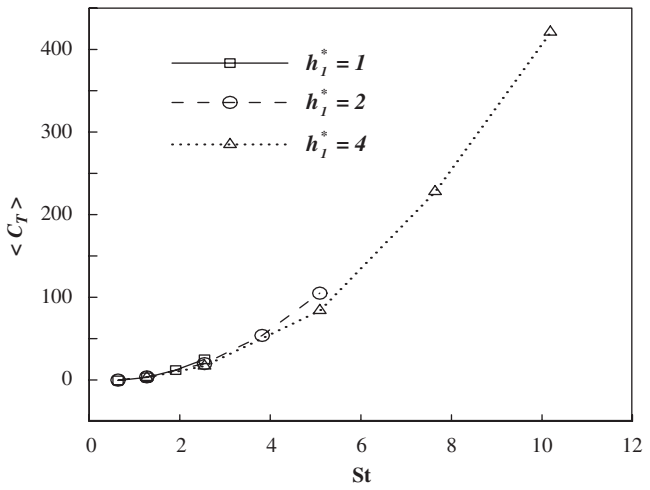

Fig. 7. Average thrust coefficient as function of the Strouhal number for different normalized heave amplitudes at Re = 1000 and $T_{lp}^* = T_{lr}^* = 0$.

number. It is known that a bluff body moving in a uniform flow will experience a drag force proportional to the squared velocity of the body relative to the flow if the form drag dominates. The foil in broadside orientation during the power stroke behaves like a bluff body moving relative to the fluid flow at a velocity of $(V_p - U_\infty)$. The normalized maximal relative velocity can be derived from Eq. (18) as

$$V_p^* - 1 = 2.5\,\text{St} - 1. \tag{33}$$

Therefore the above result is not surprising because the drag (thrust) coefficient will be proportional to St^2 for large St. Note that average thrust coefficient is negative for the cases with $k\,h_1^* = 2$ (St = 0.637), though the maximal heaving

velocity still exceeds the inflow velocity [see Eq. (33)]. This fact can be attributed to the lower heaving velocities in the acceleration and the deceleration phase respectively, at the early and the final stage of power stroke.

Fig. 8 shows the average lift coefficient as function of the Strouhal number for different normalized heave amplitudes. The data collapse is also very good. It features the positive lift force, except for the case with $k = 6$, $h_1^* = 4$ (St = 7.639). However, in comparison with the thrust force, the lift force can be disregarded more reasonably as the Strouhal number reaches a larger value.

Fig. 9 shows the thrust efficiency as function of the Strouhal number for different normalized heave amplitudes. To study the trend, cases with negative efficiency due to negative thrust mentioned above observed at $kh_1^* = 2$ are not shown. If lower amplitude ($h_1^* = 1$) discarded, the data collapse is good and thrust efficiency decreases with increasing Strouhal number. For lower normalized heave amplitude ($h_1^* = 1$), thrust efficiency exhibits irregular variation. The maximal reachable efficiency is about 0.2 at $k = 1$ and $h_1^* = 4$ (St = 1.273). Finally, for constant St, the thrust efficiency decreases with increasing k though the maximal heaving velocity keeps constant as indicated in Eq. (18). It is argued that higher acceleration and shorter amplitude of heave motion due to higher reduced frequency causes more complex flow fields and more energy lost in the fluid kinetic energy, thus reducing the efficiency.

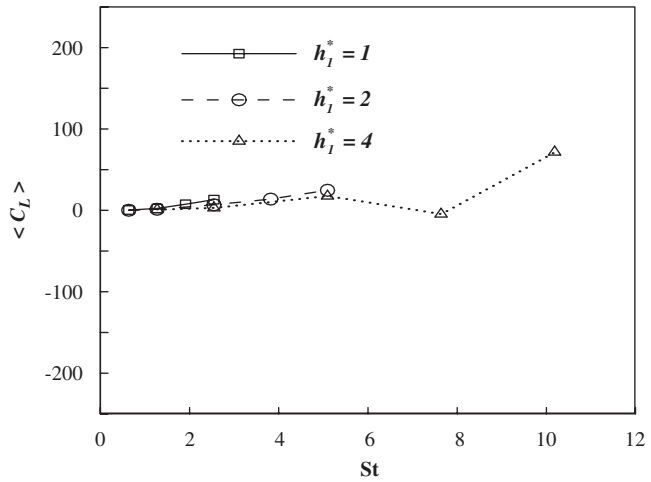

Fig. 8. Average lift coefficient as function of the Strouhal number for different normalized heave amplitudes at Re = 1000 and $T_{lp}^* = T_{lr}^* = 0$.

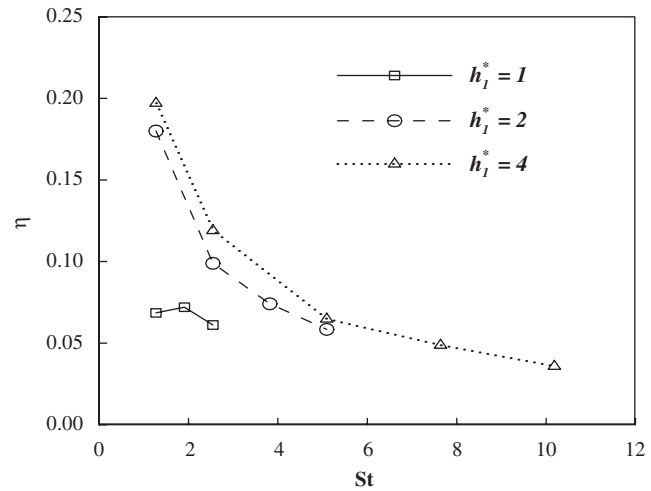

Fig. 9. Thrust efficiency as function of the Strouhal number for different normalized heave amplitudes at Re = 1000 and $T_{lp}^* = T_{lr}^* = 0$.

6.3. Effect of normalized time lags T^*_{lp} and T^*_{lr}

Because the second highest thrust efficiency at Re = 1000 is found in the case of $k = 2$ and $h^*_1 = 2$ with $T^*_{lp} = T^*_{lr} = 0$ (Fig. 9), the effect of T^*_{lp} and T^*_{lr} at this Reynolds number is examined for this combination of k and h^*_1. The combination of $k = 1$ and $h^*_1 = 4$ produces the highest efficiency, but the extra long heave amplitude would be rarely found in practice. Hence the study of this amplitude was abandoned for that of $h^*_1 = 2$. In fact, from the mechanisms of how these two time lags influence the hydrodynamic performances, as discussed later, the conclusion drawn about the effect of these two time lags is not supposed to change with the design parameters, at least for this Reynolds number.

Before studying their effects, some particular numerical values are mentioned due to relevance to the characteristics of the rowing kinematics. That is, for $T^*_{lp} = -0.05$, the feathered-to-broadside rotation is started exactly when the deceleration phase of the recovery stroke begins and the rotation is completed exactly at the end of the recovery stroke; for $T^*_{lp} = 0.05$, the rotation starting is delayed until the end of the recovery stroke and the fully broadside orientation is attained at the end of the acceleration phase of the power stroke. Similarly, for $T^*_{lr} = -0.05$, the broadside-to-feathered rotation is started exactly when the deceleration phase of the power stroke begins and the rotation is finished just at the end of the power stroke; for $T^*_{lr} = 0.05$, the broadside-to-feathered rotation is delayed until the end of the power stroke and the fully feathered orientation is attained at the end of the acceleration phase of the recovery stroke.

Fig. 10 presents the average thrust coefficient as function of T^*_{lp} for different T^*_{lr}. For any given T^*_{lr}, except for $T^*_{lr} = 0.05$, the average thrust coefficient increases with T^*_{lp}. For any given T^*_{lp}, the average thrust coefficient increases as T^*_{lr} is lowered down from 0.05 to −0.1. If the broadside-to-feathered rotation is started further earlier ($T^*_{lr} = -0.15$), the average thrust coefficient can not be augmented any more. Conversely, it comes back near the curve for $T^*_{lr} = -0.05$. Thus, the thrust hits maximum for the case of $T^*_{lp} = 0.1$ and $T^*_{lr} = -0.1$ and the minimum (negative value) for the case of $T^*_{lp} = -0.05$ and $T^*_{lr} = 0.05$. A brief conclusion can be drawn from this figure that, in general, larger thrust would be acquired if the feathered-to-broadside rotation is started after the beginning of the power stroke and the broadside-to-feathered rotation is finished before the end of the power stroke.

Fig. 11 presents the average lift coefficient as function of T^*_{lp} for different T^*_{lr}. For any given T^*_{lr}, except for $T^*_{lr} = 0$, the average lift coefficient increases with T^*_{lp}. However, there is no definite rule for the variation of the average lift coefficient with T^*_{lr} for any given T^*_{lp}. It is noted that most cases produce positive lift with the maximum being generated in the case of $T^*_{lp} = 0.1$ and $T^*_{lr} = -0.15$. The ratio of lift to thrust is about 0.516 for this case.

Fig. 12 presents the thrust efficiency as function of T^*_{lp} for different T^*_{lr}. For any given T^*_{lp}, the thrust efficiency increases as T^*_{lr} is lowered down from 0.05 to −0.05. The values of thrust efficiency in the curves for $T^*_{lr} = -0.15$ and $T^*_{lr} = -0.1$ are nearly the same as those in the curve for $T^*_{lr} = -0.05$. Thus, the thrust efficiency hits the maximum (0.274) for the case of $T^*_{lp} = 0.05$ and $T^*_{lr} = -0.05$ and the minimum (−0.016) for the case of $T^*_{lp} = -0.05$ and

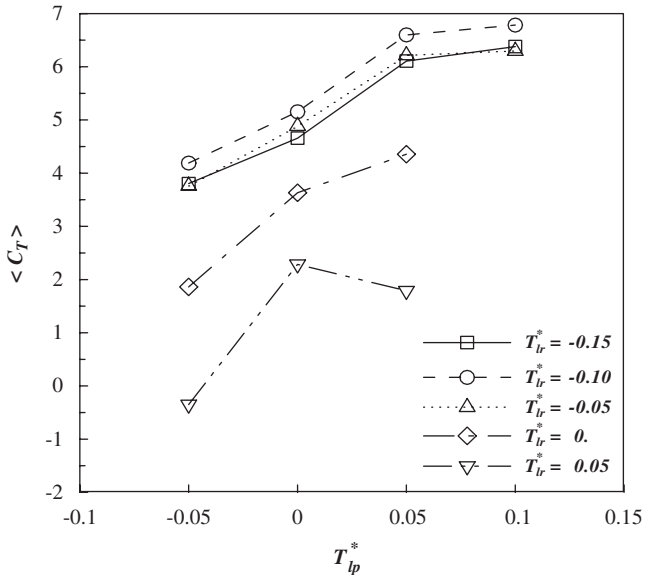

Fig. 10. Average thrust coefficient as function of T^*_{lp} for different T^*_{lr} at Re = 1000, $k = 2$ and $h^*_1 = 2$.

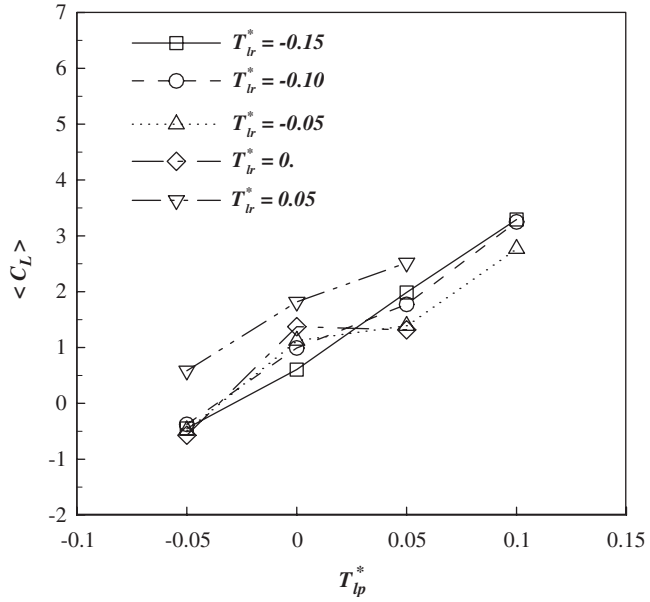

Fig. 11. Average lift coefficient as function of T^*_{lp} for different T^*_{lr} at Re = 1000, $k = 2$ and $h^*_1 = 2$.

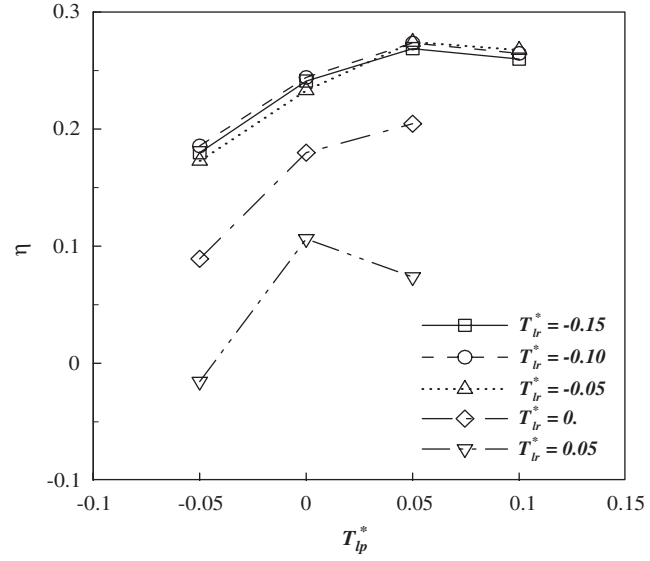

Fig. 12. Thrust efficiency as function of T^*_{lp} for different T^*_{lr} at Re = 1000, $k = 2$ and $h^*_1 = 2$.

$T^*_{lr} = 0.05$. The overall pattern of variation resembles that for the average thrust coefficient. Thus, larger efficiency would be attained if the feathered-to-broadside rotation is started "right" after the beginning of the power stroke and the broadside-to-feathered rotation is finished "right" before the end of the power stroke.

To understand the mechanisms how these time lags influence the hydrodynamic performance, the transient behavior of the force and moment coefficients in two opposite cases were examined. The first case is $T^*_{lp} = 0.05$ and $T^*_{lr} = -0.05$ and the second $T^*_{lp} = -0.05$ and $T^*_{lr} = 0.05$. Fig. 13 shows the thrust coefficient as function of normalized time for these two cases. It can be seen that major differences between the two cases are found in the acceleration and the deceleration phase of the heave motion. In the acceleration phase of the power stroke ($t/T_{\text{cycle}} = 0$–0.1), for Case 1, the foil rotates from the feathered to the broadside orientation; for Case 2, the foil keeps broadside oriented through the phase. The

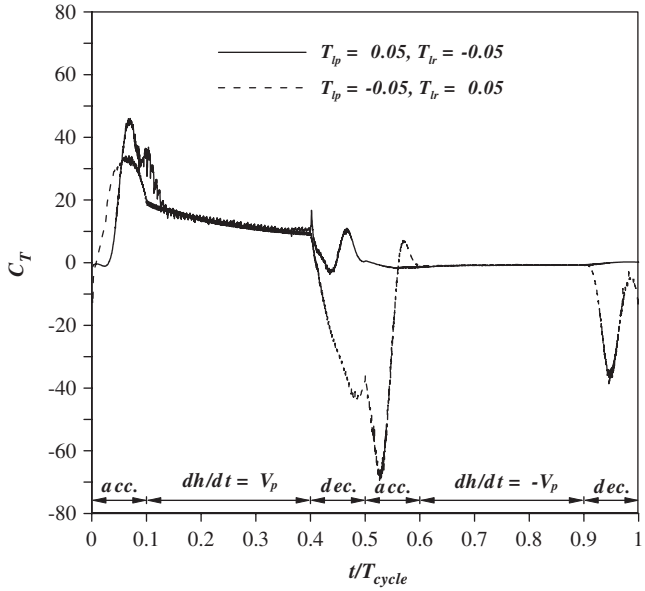

Fig. 13. Thrust coefficient as function of normalized time for two combinations of T^*_{lp} and T^*_{lr} at Re = 1000, $k = 2$ and $h^*_1 = 2$.

combination of rotational and linear motions in Case 1 causes larger peak thrust than the purely linear motion in Case 2 does. In the constant-velocity phase of the power stroke ($t/T_{\text{cycle}} = 0.1$–0.4), the two cases differ little. When the foil motion falls into the deceleration phase of the power stroke ($t/T_{\text{cycle}} = 0.4$–0.5), abrupt drops in thrust can be observed for both cases. This thrust drop is mainly due to the inertia force on the foil exerted by the fluid on the upstream side of the foil ($-x$ side in this work). This phenomenon can be interpreted in terms of the accelerated fluid impacting on the relatively fixed foil. However, the broadside-to-feathered rotation of Case 1 alleviates this inertia impact, hence not lowering the thrust as much as Case 2. At the end of the power stroke, the acceleration phase of the recovery stroke ($t/T_{\text{cycle}} = 0.5$–0.6) starts. In this phase, the thrust is nearly zero for Case 1 because the foil is fully feathered oriented; however, the thrust is first reduced further and then rises up to nearly zero for Case 2 because the foil undergoes and completes the broadside-to-feathered orientation in this phase. In the constant-velocity phase of the recovery stroke ($t/T_{\text{cycle}} = 0.6$–0.9), nearly zero thrust is generated for both cases due to the fully feathered orientation. Finally, in the deceleration phase of the recovery stroke ($t/T_{\text{cycle}} = 0.9$–1), thrust is nearly zero for Case 1 due to the foil being still in the fully feathered orientation; for Case 2, the interplay of the inflow velocity, the linear velocity and deceleration of foil, and the change of orientation produces a negative thrust with an initial drop and a later rise. Eventually, the average thrust of Case 1 is much larger than that (negative value) of Case 2 as shown in Fig. 10.

For the thrust efficiency, the moment coefficient as function of normalized time for these two cases, as shown in Fig. 14, is also required to analyze the corresponding average mechanical power. First, look into the contribution of thrust to the average mechanical power by inspecting Fig. 13 again. Because significant differences between the two cases occur only in the acceleration and the deceleration phase of the heave motion, especially early in the acceleration phase and late in the deceleration phase, the average mechanical power due to thrust differs little between the two cases as implied in Eq. (22), considering the low heaving velocity in these phases. Then, turning to the contribution of moment to the average mechanical power, the curve for the moment coefficient of one case is basically the time-shifted (lead or lag) one of the other case, as shown in Fig. 14. For the power-to-recovery stroke switch, Case 1 leads Case 2 while for the recovery-to-power stroke switch, Case 1 lags behind Case 2. Because the time lead or lag is synchronous with the kinematic one, i.e., T^*_{lp} and T^*_{lr}, the average mechanical power due to moment differs little between the two cases as implied in Eq. (22). In summary, there would not be large difference in the average mechanical power between the two cases. In fact, the average mechanical power coefficients of Cases 1 and 2 are 22.6 and 22.4, respectively. Thus, the thrust efficiency as function of T^*_{lp} and T^*_{lr} has the same characteristics as the thrust coefficient as implied in Eq. (23).

Fig. 15 presents the vorticity contour at selected instants in the power stroke for these two cases. For Case 1, it can be seen that, when the foil is oriented broadside, the vortex flow structures are asymmetrical about the x-axis because the earlier feathered-to-broadside rotation. Approaching the end of the power stroke, a strong vortex is generated above the foil due to the broadside-to-feathered rotation. However, the thrust is hardly affected because the foil is nearly

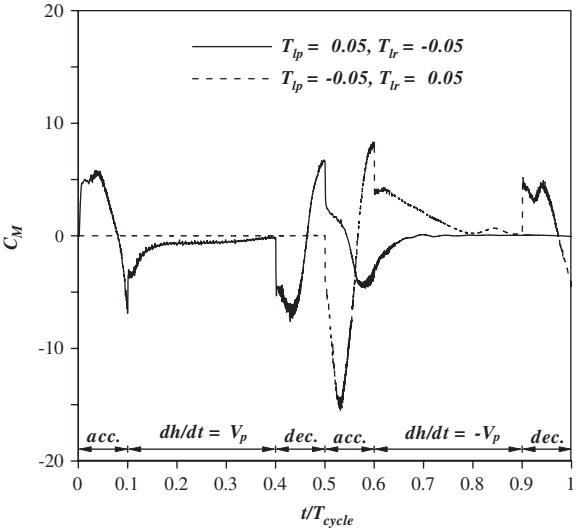

Fig. 14. Moment coefficient as function of normalized time for two combinations of T^*_{lp} and T^*_{lr} at Re = 1000, $k = 2$ and $h^*_1 = 2$.

feathered oriented. For Case 2, it can be seen that a symmetric vortex pair is attached to the foil on the upstream side through this stroke. Besides, another vortex pair on the downstream side is clearly formed approaching the end of the power stroke because of the inertia impact by the upstream fluid on the foil due to foil deceleration mentioned above.

Fig. 16 presents the vorticity contour at selected instants in the recovery stroke for these two cases. For Case 1, due to the feathered orientation, the vortex flow structures inherited from the power stroke are gradually dissipated in the flow and eventually left behind by the foil. For Case 2, because all the changes of orientation occur in this stroke, strong vortices are newly generated and the vortex flow structures are more complicated than those of Case 1. Note that a large negative thrust can be easily linked to the vortical structures at $t/T_{\text{cycle}} = 0.52$.

6.4. Effect of Reynolds number

To examine the effect of Reynolds number, the design parameters of $k = 2$ and $h^*_1 = 2$ with $T^*_{lp} = 0.05$ and $T^*_{lr} = -0.05$ were selected to perform simulations at Re = 10, 50, 100, 500, and 1000. Fig. 17 presents the computed average thrust coefficient as function of Re. It can be observed that the average thrust coefficient increases rapidly with Re at very low Re and enters on a plateau approaching higher Re. Further scrutinizing the transient thrust decomposed into the pressure part and the viscous part (Fig. 18), the latter is affected by Reynolds number much stronger than the former in the recovery stroke. The viscous force exerted on the foil in the recovery stroke (negative thrust) grows with decreasing Re. The growth rate is larger for smaller Re, hence explaining the rapid reduction of the thrust with decreasing Re.

From the similarity solution of laminar flow over a flat plate (Blasius, 1908), an important problem in the boundary layer theory, it is known that the viscous drag coefficient ($C_{D,\text{rel}}$) is related to the Reynolds number (Re_{rel}) as

$$C_{D,\text{rel}} = 2.676\text{Re}_{\text{rel}}^{-1/2}, \tag{34}$$

where

$$C_{D,\text{rel}} \equiv 2D/\rho V_{\text{rel}}^2 c, \tag{35}$$

$$\text{Re}_{\text{rel}} \equiv V_{\text{rel}} c/\nu, \tag{36}$$

with D being the drag force and V_{rel} the relative free-stream velocity. Note that the numerics, 2.676, in the right-hand side of Eq. (34) has reflected the fact that the plate experiences the viscous force both on the top and bottom surfaces. In the most part of the recovery stroke, $V_{\text{rel}} = V_p + U_\infty$, that is, $V^*_{\text{rel}} \equiv V_{\text{rel}}/U_\infty = V^*_p + 1$. Being aware of the different definitions of the force coefficient and the Reynolds number in the present work, the following relation can be derived

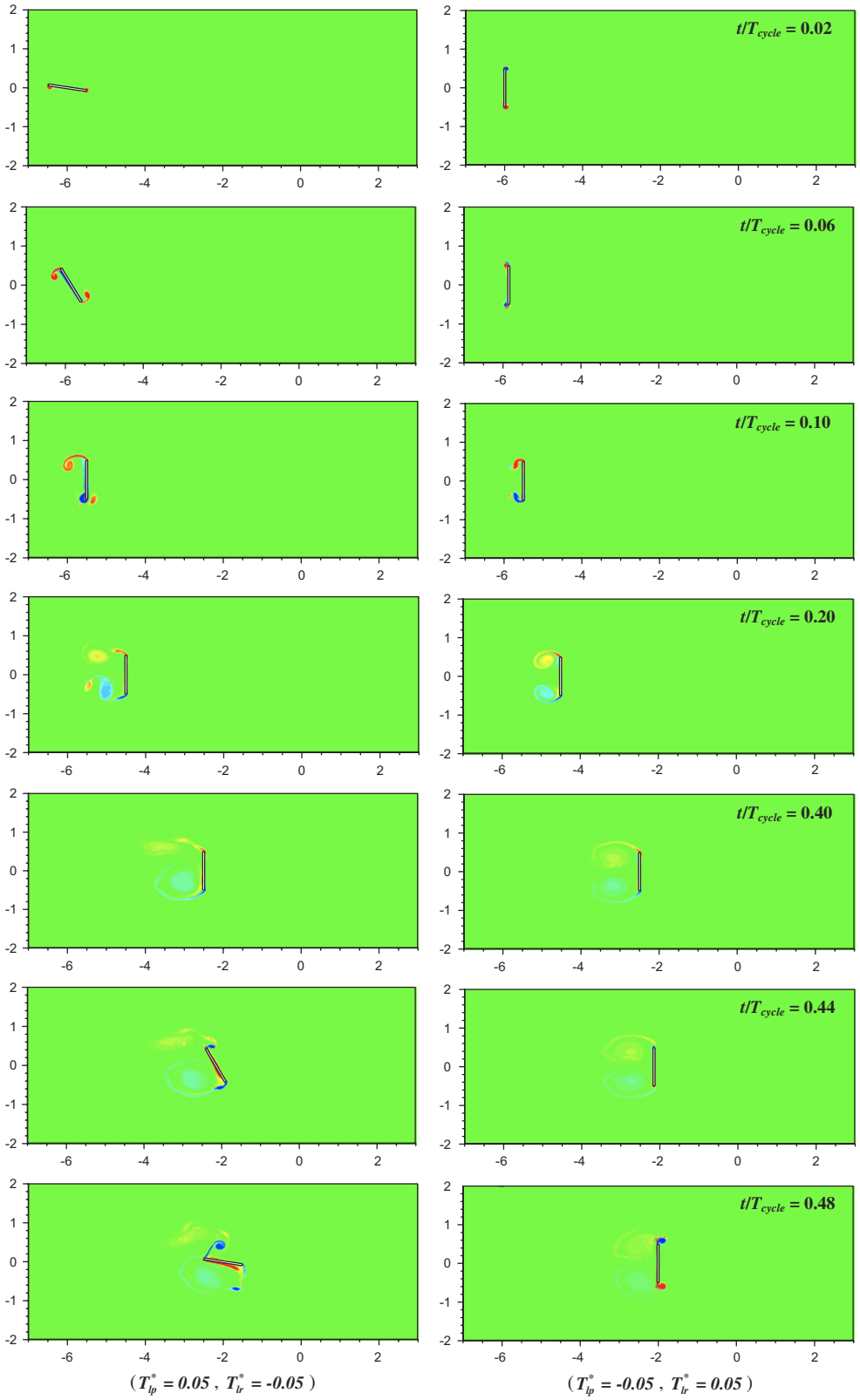

Fig. 15. Vorticity contour at selected instants in the power stroke for two combinations of T^*_{lp} and T^*_{lr} at Re = 1000, $k = 2$ and $h^*_1 = 2$.

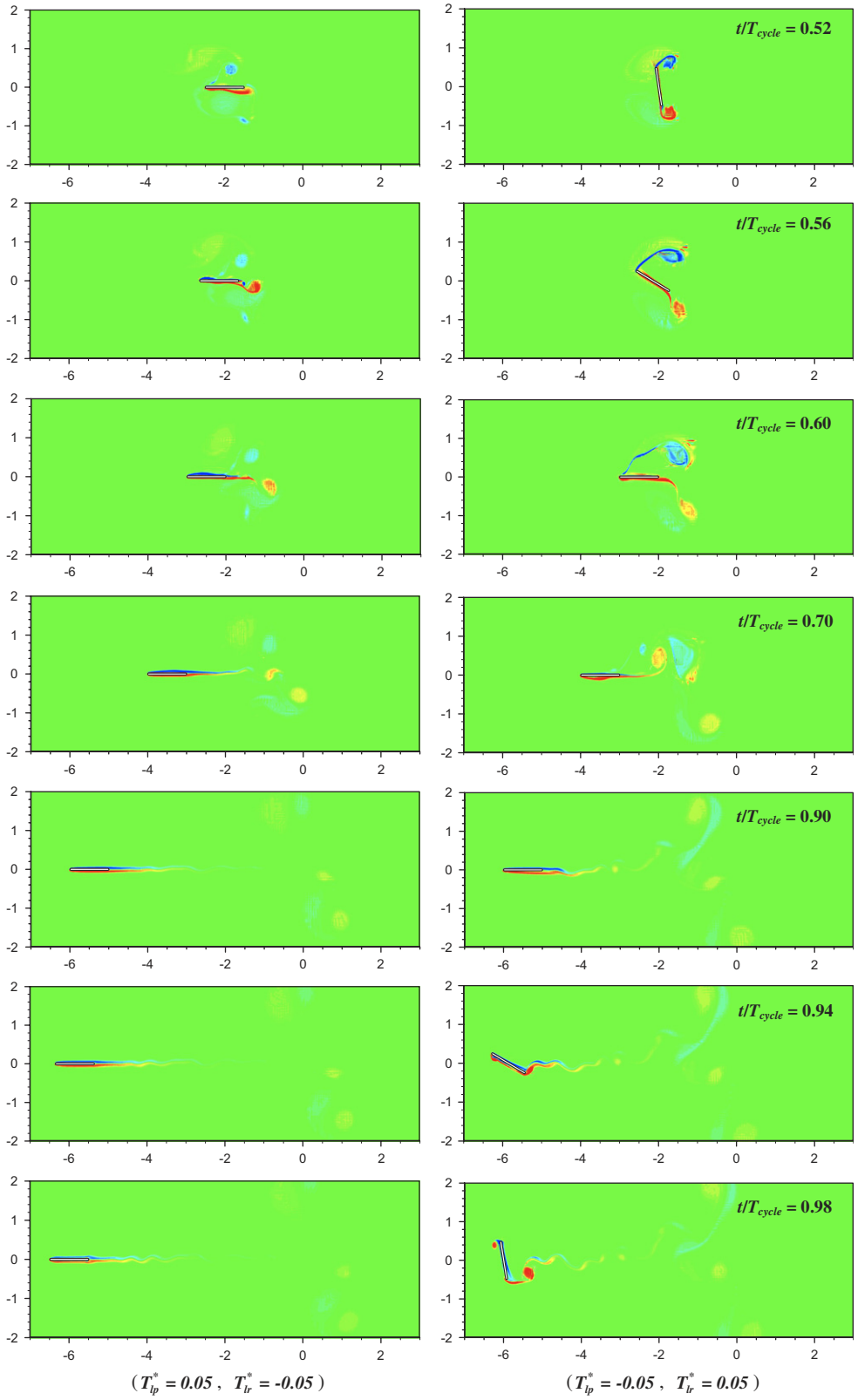

Fig. 16. Vorticity contour at selected instants in the recovery stroke for two combinations of T^*_{lp} and T^*_{lr} at Re = 1000, $k = 2$ and $h^*_1 = 2$.

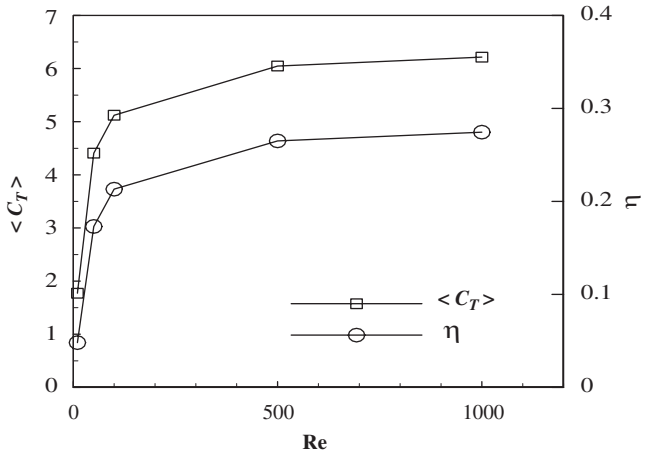

Fig. 17. Average thrust coefficient and efficiency as function of Re for the case of $k = 2$ and $h_1^* = 2$ with $T_{lp}^* = 0.05$ and $T_{lr}^* = -0.05$.

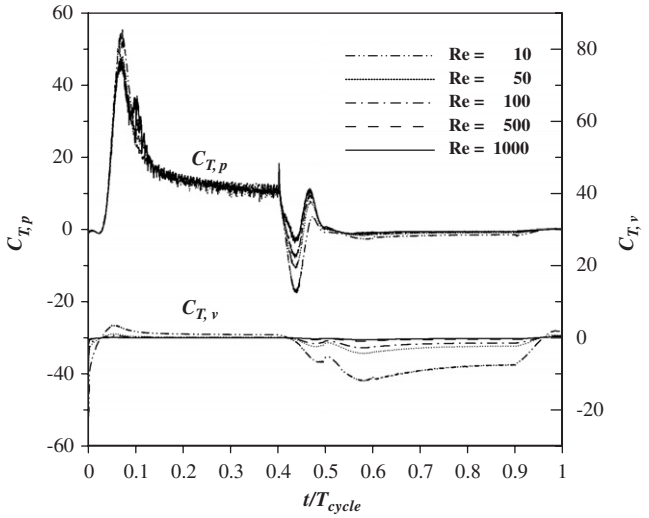

Fig. 18. Thrust coefficient due to pressure and viscous force as function of normalized time at different Re for the case of $k = 2$ and $h_1^* = 2$ with $T_{lp}^* = 0.05$ and $T_{lr}^* = -0.05$.

from Eqs. (34)–(36):

$$\frac{\partial C_T}{\partial \mathrm{Re}} = 1.338\left(\frac{V_{\mathrm{rel}}^*}{\mathrm{Re}}\right)^{3/2}, \tag{37}$$

showing that the growth rate increases with decreasing Re. For $k = 2$ and $h_1^* = 2$, this slope is calculated to be 0.362, 0.032, and 0.011 for Re = 10, 50 and 100, respectively. In Fig. 17, the slope is 0.066 between Re = 10 and 50 and 0.02 between Re = 50 and 100, both consistent with those calculated above. This simple model also indirectly assures the reliable simulations in the present work.

Similar trends exist in the thrust efficiency as function of Re as shown in Fig. 17. The reason is that the contribution of the moment to the mechanical power, due to either pressure or viscous force, is almost the same for different Reynolds numbers, as shown in Fig. 19.

In a brief summary, the effect of Reynolds number manifests itself mainly in terms of the viscous force exerted on the foil in the recovery stroke.

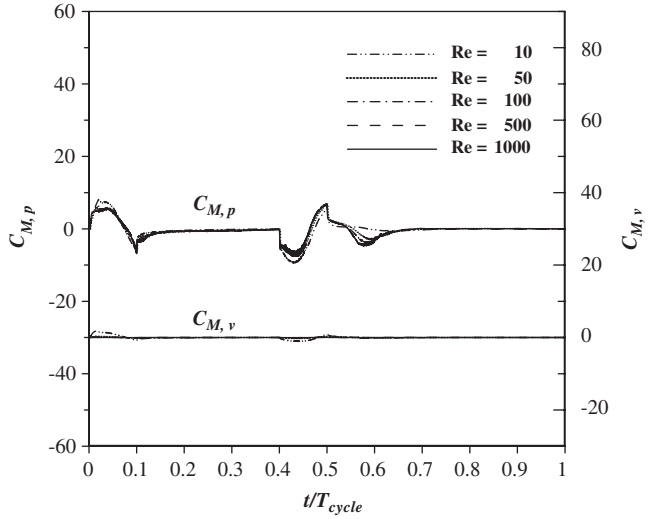

Fig. 19. Moment coefficient due to pressure and viscous force as function of normalized time at different Re for the case of $k = 2$ and $h_1^* = 2$ with $T_{lp}^* = 0.05$ and $T_{lr}^* = -0.05$.

7. Conclusions

In this paper, the hydrodynamic performance of a 2-D flat-plate hydrofoil in rowing motion is numerically studied by a Cartesian grid method with the cut-cell approach. The design parameters studied are the reduced frequency of the rowing motion, the amplitude of the heave motion, and the time lags of the feathered-to-broadside rotation and the broadside-to-feathered rotation.

The major conclusions drawn from the simulation results are as follows. Both the average thrust coefficient and the average lift coefficient exhibit very good data collapse as function of Strouhal number. Further, the former correlates very well (in a quadratic manner) with the Strouhal number. Positive average lift force is generated for most cases subject to the proposed rowing kinematics. For a constant maximal heaving velocity, the thrust efficiency decreases with increasing reduced frequency. For the reduced frequency and the normalized heave amplitude fixed, larger thrust and efficiency can be attained if the feathered-to-broadside rotation is started right after the beginning of the power stroke and the broadside-to-feathered rotation is finished right before the end of the power stroke. Finally, both thrust and efficiency increase with Re.

Acknowledgments

This work is partly supported by the Grant NSC 96-2221-E-022-001. The reviewers of the manuscript are gratefully acknowledged for their valuable comments and suggestions, especially those regarding flux treatment of mesh refinement.

Appendix A

The interpolation scheme at the coarse–fine cell interface for the solution variable and its normal derivative is devised for the sake of easy implementation. Theoretically, the order of accuracy is two and one for the solution variable and its normal derivative, respectively. For illustration, the following test problem is solved and the results compared with the exact solution:

$$\nabla^2 \Phi = -8\pi^2 \sin(2\pi x)\cos(2\pi y) \text{ in the domain } [0,1]\times[0,1], \tag{38}$$

$$\Phi(0,y) = \Phi(1,y) = 0 \quad \text{and}$$
$$\Phi(x,0) = \Phi(x,1) = \sin(2\pi x). \tag{39}$$

The exact solution is $\Phi(x,y) = \sin(2\pi x)\cos(2\pi y)$.

Three grids were used for grid-independence test. Each has two levels of refinement of which the interface consists of four sides of the square $[0.25, 0.75] \times [0.25, 0.75]$. The coarsest grid has two mesh sizes, $\frac{1}{64}$ and $\frac{1}{32}$, and 128 cell interfaces as shown in Fig. A.1. The corresponding numerics for the middle and finest grid are ($\frac{1}{128}$, $\frac{1}{64}$, 256) and ($\frac{1}{256}$, $\frac{1}{128}$, 512) respectively. For any quantity f, The L_2-norm error is defined as

$$\varepsilon = \frac{1}{N_{\text{interface}}} \sqrt{\sum_{i=1}^{N_{\text{interface}}} (f_{i,\text{cal}} - f_{i,\text{exact}})^2}, \tag{40}$$

where $N_{\text{interface}}$ is the total number of coarse–fine cell interfaces. $f_{i,\text{cal}}$ and $f_{i,\text{exact}}$ are calculated and exact values, respectively, at the center of the ith interface. For the present grid-independence test, f is taken as Φ or $\mathrm{d}\Phi/\mathrm{d}n$ where n denotes the normal direction of the interface.

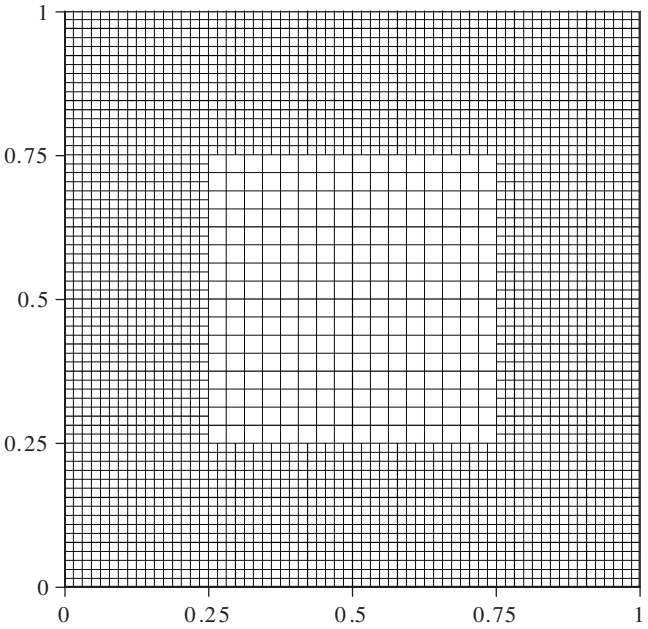

Fig. A.1. The coarsest grid for grid-independence test of the interpolation scheme employed at the coarse–fine cell interface.

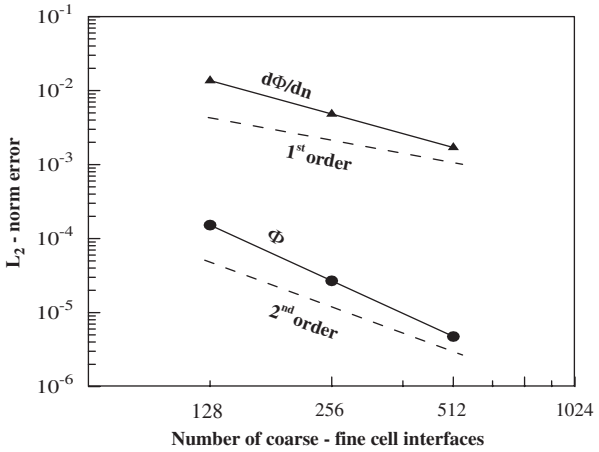

Fig. A.2. Result of grid-independence test of the interpolation scheme employed at the coarse–fine cell interface. The test problem is the Poisson equation $\nabla^2\Phi = -8\pi^2 \sin(2\pi x)\cos(2\pi y)$ in the domain $[0, 1] \times [0, 1]$ with $\Phi(0, y) = \Phi(1, y) = 0$ and $\Phi(x, 0) = \Phi(x, 1) = \sin(2\pi x)$. The dashed lines indicate the first- and second-order convergence.

Fig. A.2 depicts the result of grid-independence test, showing better than second-order accuracy for Φ and better than first-order accuracy for $d\Phi/dn$.

References

Anderson, J.M., 1996. Vortex control for efficient propulsion. Ph.D. dissertation, Massachusetts Institute of Technology, Cambridge, MA.

Antiochos, S.K., MacNeice, P.J., Spicer, D.S., Klimchuk, J.A., 1999. The dynamic formation of prominence condensations. Astrophysical Journal 512, 985–991.

Blake, R.W., 1983. Median and paired fin propulsion. In: Webb, P.W., Weihs, D. (Eds.), Fish Biomechanics. Praeger Publishers, New York.

Blasius, H., 1908. Grenzschichten in flüssigkeiten mit kleiner reibung. Zeitschrift für angewandte Mathematik und Physik. Journal of Applied Mathematics and Physics 56, 1–37 (Translation, NACA TM 1256).

Breder, C.M., 1926. The locomotion of fishes. Zoologica 4, 159–256.

Chung, M.-H., 2006. Cartesian cut cell approach for simulating incompressible flows with rigid bodies of arbitrary shape. Computers and Fluids 35 (6), 607–623.

Harper, D.G., Blake, R.W., 1990. Fast-start performance of rainbow trout Salmo Gairdneri and northern pike Esox Lucius. Journal of Experimental Biology 150, 321–342.

Isogai, K., Shinmoto, Y., Watanabe, Y., 1999. Effects of dynamic stall on propulsive efficiency and thrust of flapping airfoil. AIAA Journal 37 (10), 1145–1151.

Koochesfahani, M.M., 1987. Vortical patterns in the wake of an oscillating airfoil. Presented at the AIAA 25th Aerospace Sciences Meeting, Reno, NV, USA.

Lighthill, M.J., 1975. Mathematical Biofluiddynamics. Society for Applied and Industrial Mathematics, Philadelphia.

Lindsey, C.C., 1978. Form, function and locomotory habits in fish. In: Hoar, W.S., Randall, D.J. (Eds.), Fish Physiology Locomotion, Vol. VII. Academic Press, New York.

MacNeice, P., Olson, K.M., Mobarry, C., deFainchtein, R., Packer, C., 2000. PARAMESH: a parallel adaptive mesh refinement community toolkit. Computer Physics Communications 126, 330–354.

Mittal, R., 2004. Computational modeling in biohydrodynamics: trends, challenges, and recent advances. IEEE Journal of Oceanic Engineering 29 (3), 595–604.

Ramamurti, R., Sandberg, W.C., Löhner, R., 2001. Simulation of flow about flapping airfoils using a finite element incompressible flow solver. AIAA Journal 39, 253–260.

Saad, Y., Schultz, M.H., 1986. GMRES: a generalized minimal residual algorithm for solving nonsymmetric linear systems. SIAM Journal on Scientific and Statistical Computing 7, 856–869.

Triantafyllou, M.S., Techet, A.H., Hover, F.S., 2004. Review of experimental work in biomimetic foils. IEEE Journal of Oceanic Engineering 29 (3), 585–594.

Tuncer, I.H., Platzer, M.F., 2000. Computational study of flapping airfoil aerodynamics. AIAA Journal of Aircraft 37 (3), 514–520.

Udaykumar, H.S., Mittal, R., Shyy, W., 1999. Solid–liquid phase front computations in the sharp interface limit on fixed grids. Journal of Computational Physics 153, 535–574.

Videler, J.J., 1993. Fish Swimming. Chapman & Hall, London.

Vogel, S., 1996. Life in Moving Fluids: The Physical Biology of Flow, Second ed. Princeton University Press, Princeton.

Walker, J.A., Westneat, M.W., 2000. Mechanical performance of aquatic rowing and flying. Proceedings of the Royal Society of London, Series B 267, 1875–1881.

Walker, J.A., Westneat, M.W., 2002. Performance limits of labriform propulsion and correlates with fin shape and motion. Journal of Experimental Biology 205, 177–187.

Wang, Z.J., 2000. Vortex shedding and frequency selection in flapping flight. Journal of Fluid Mechanics 410, 323–341.

Webb, P.W., 1986. Effect of body form and response threshold on the vulnerability of four species of teleost attacked by largemouth bass (*Micropterus salmoides*). Canadian Journal of Fisheries and Aquatic Science 43, 763–771.

Weihs, D., 1973. The mechanism of rapid starting of slender fish. Biorheology 10, 343–350.